An interpretable formula for lattice thermal conductivity in crystals

Xiaoying Wang[1], Guoyu Shu,[1] Guimei Zhu,[2] Jian-Sheng Wang,[3] Jun Sun,[1] Xiangdong Ding,[1] Baowen Li[4,‡], and Zhibin Gao,[1,†]

[1]State Key Laboratory for Mechanical Behavior of Materials, School of Materials Science and Engineering, Xi'an Jiaotong University, Xi'an 710049, China

[2]School of Microelectronics, Southern University of Science and Technology, Shenzhen, 518055, China

[3]Department of Physics, National University of Singapore, Singapore 117551, Republic of Singapore

[4]Department of Physics, Department of Materials Science and Engineering, Southern University of Science and Technology, Shenzhen 518055, PR China

‡ E-mail: libw@sustech.edu.cn

† E-mail: zhibin.gao@xjtu.edu.cn

1. Self-consistent phonon theory

Self-consistent phonon (SCPH) theory [1] is a methodology that can rigorously account for quartic anharmonicity phonon renormalization effects beyond perturbation theory. It considers the quantum effect of phonons and can better describe the strong anharmonicity and atomic interaction. In brief, the SCPH can be written as [2,3].

$$\Omega_\lambda^2 = \omega_\lambda^2 + 2\Omega_\lambda \sum_{\lambda_1} I_{\lambda\lambda_1} \tag{1}$$

where ω_λ is the original phonon frequency from the harmonic approximation and Ω_λ is the temperature-dependent renormalized phonon frequency. The scalar $I_{\lambda\lambda_1}$ can be obtained by

$$I_{\lambda\lambda_1} = \frac{h}{8N_0} \frac{V^{(4)}(\lambda,-\lambda,\lambda,-\lambda_1)}{\Omega_\lambda \Omega_{\lambda_1}} [1+2n_\lambda(\Omega_{\lambda_1})] \tag{2}$$

in which $V^{(4)}$ is the fourth-order IFCs in the reciprocal representation and phonon population n_λ satisfies Bose-Einstein distribution as a function of temperature. Both Eq. (1) and Eq. (2) have parameters $I_{\lambda\lambda_1}$ and Ω_λ in common, and thus SCPH equation can be solved iteratively. Note that $I_{\lambda\lambda_1}$ can be interpreted as the interaction between a pair of phonon modes, λ, and

λ_1 including the temperature effects [4]. Therefore, we need to take into account SCPH considering temperature effects and quartic anharmonicity renormalization that estimates κ_L accurately.

2. **Pearson correlation coefficient**

In this work, the Pearson correlation coefficient (PCC) was employed to evaluate the correlation between basic physical parameters and the lattice thermal conductivity κ_L. PCC is a statistical metric that measures the degree of a linear relationship between two random variables with a value between -1 and 1. It has a wide range of applications in statistical analysis, machine learning, and data mining. We hypothesize that *X* and *Y* are two zero-mean real-valued random variables, PCC can be described as,

$$\mathrm{r}(X,Y)=\frac{\mathrm{cov}(X,Y)}{\sqrt{D(X)}\sqrt{D(Y)}} \tag{3}$$

where covariance of X and Y is,

$$\begin{aligned}&\mathrm{cov}(X,Y)=E(X-E(X))(Y-E(Y)),\\&=E(X,Y)-E(X)E(Y),\\&=\frac{1}{n}\sum_{i=1}^{n}x_iy_i-(\sum_{i=1}^{n}x_i)(\sum_{i=1}^{n}y_i),\end{aligned} \tag{4}$$

in which *n* is the index of number. x_i and y_i are the data for *i*-th number of $\{X_i\}$ and $\{Y_i\}$. Squared difference *D(X)* is written as,

$$\begin{aligned}&\mathrm{D}(X)=E((X-E(X))^2),\\&=E(X^2)-E^2(X),\\&=\frac{1}{n^2}(n\sum_{i=1}^{n}x_i^2-(\sum_{i=1}^{n}x_i)^2).\end{aligned} \tag{5}$$

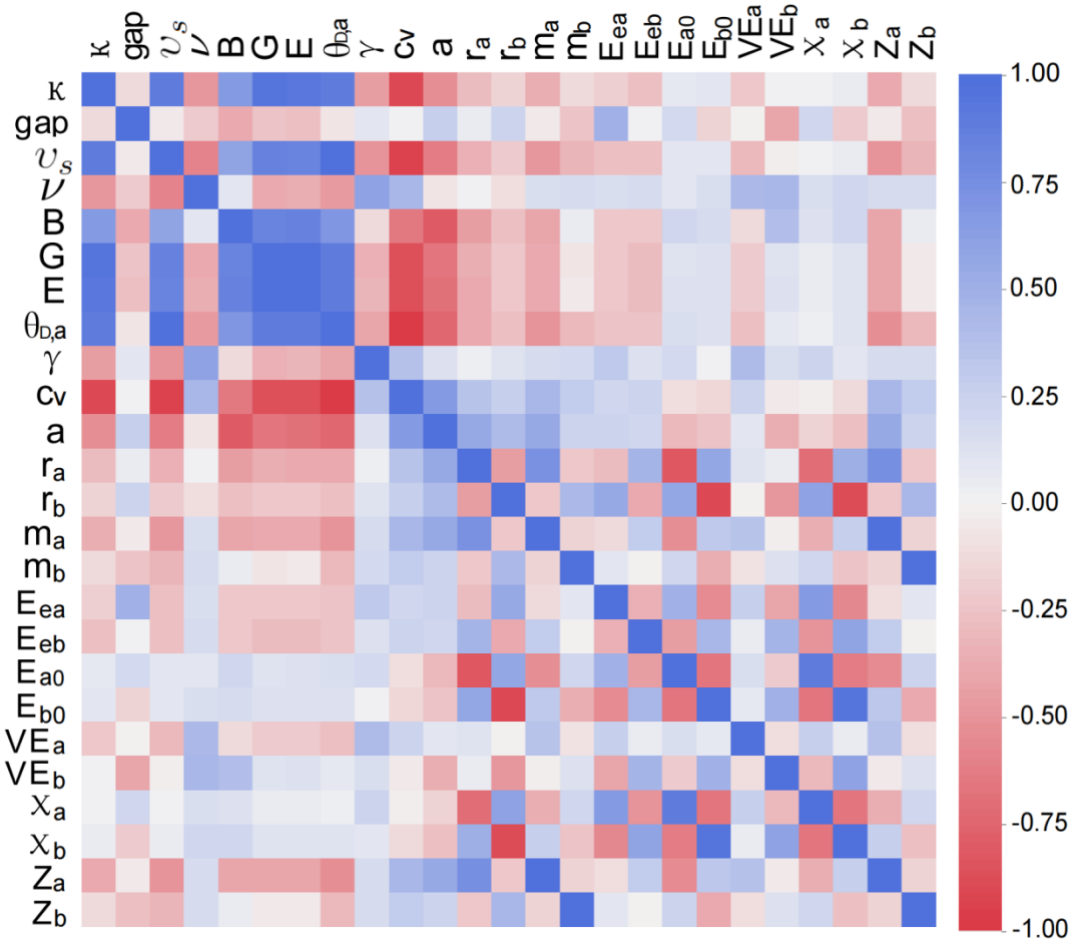

FIG. S1. Pearson correlation coefficient (PCC) between lattice thermal conductivity κ_L, electronic band gap, speed of sound v_s, Poisson's ratio ν, bulk modulus B, shear modulus G, Young's modulus E, Debye temperature $\theta_{D,a}$, Grüneisen parameter γ, heat capacity Cv, lattice constant a, their atomic radius r_a, r_b, their atomic mass m_a, m_b, their electron affinity E_{ea}, E_{eb}, their ground state energy per atoms E_{a0}, E_{b0}, their number of valence electrons VE_a, VE_b, their electronegativities χ_a, χ_b, their atomic number of atoms Z_a, Z_b for nonmetallic crystals. The blue section is a positive correlation, while the red one is a negative correlation.

3. Computational techniques

To verify the accuracy of our proposed model compared with the DFT theoretical calculation, we utilized *ab initio* density functional theory (DFT) as implemented in *Vienna ab initio simulation package* (VASP) combined with projector-augmented wave (PAW) pseudopotentials [5] and the Perdew-Burke-Ernzerhof (PBE) functionals [6] employing in SiC, AgCl, $CsPbBr_3$, CdS, MgO, GaN, LiH, RbBr, RbI. Cutoff energy of 400 eV was used with 11 ×11×11 Monkhorst-Pack k-point grids in structure optimization. The self-consistent iteration for the convergence criterion was below 10−8eV, and all geometries were optimized by the conjugate-gradient method until none of the residual Hellmann-Feynman forces exceeded 10^{-6} eV/°A. Quasi-harmonic approximation was adopted to calculate the κ_L.

In order to compute the thermoelectric properties of Cs_2Se, we constructed a 2×2×2 supercell. A 9×9×9 Monkhorst-Pack *k*-grids were used to generate second- and third-order interatomic

force constants (IFCs) from phonopy [7] and CSLD [8] by the finite-displacement technique. When using CSLD to obtained FORCE CONSTANTS, we employed 10.0 Å, 8.0 Å, 7.1 Å as nearest-, second-nearest, and third-nearest neighbour, respectively. The fitting error for harmonic force-constants is 4.32%, and the fitting error for anharmonic force-constants is 7.14%. Subsequently, we ran 2000-step *ab initio* molecular dynamics (AIMD) at 300 K with 2 ps step size and selected 40 random incoherent configurations. Combining all IFCs together, κ_L and thermal transport properties considering quartic anharmonicity and self-consistent phonon can be obtained [9]. When using ShengBTE to obtain the lattice thermal conductivity, the integration grid of SCPH+3,4ph is $9\times9\times9$ in our computation, the grid of SCPH+3ph is $14\times14\times14$. Furthermore, the scale-broadening parameter we choosen is 0.5 in all thermal conductivity calculations.

The Seebeck coefficient, conductivity, and power factor were calculated by considering the electron-phonon coupling such as the acoustic deformation potential, and ionized impurity, as implemented in the AMSET package. The elastic constants, dielectric constants, deformation potential, and wave functions were gained with $12\times12\times12$ *k*-meshes. The electron relaxation time and electronic transport properties were obtained by a uniform $51\times51\times51$ *k*-point grids.

4. Description of CGCNN method

The crystal graph convolutional neural network (CGCNN) utilizes a graph representation of the crystal that is composed of two parts, (i) nodes that represent constituent atoms of the crystal, and (ii) edges that denote the bonds between neighboring atoms. A node is embedded with a vector v_i to signify the properties of atom *i*, where we define embedding as the process of mapping a discrete object to a vector of real numbers. Each edge is also embedded with a vector $u_{(i,j)k}$ that contains the distance information between neighboring atoms *i* and *j* of the crystal unit cell. In order to account for the periodicity of the crystal, multiple edges between atoms *i* and *j* as indexed by *k*, can exist. Each node in the crystal graph is connected to its 12 nearest neighbors. During the training phase, the node vectors are updated iteratively according to a convolution function defined by [10],

$$\begin{aligned} v_i^{(t+1)} &= v_i^{(t)} + \sum_{j,k} \sigma(Z_{(i,j)_k}^{(t)} W_f^{(t)} + b_f^{(t)}) \odot g(Z_{(i,j)_k}^{(t)} W_s^{(t)} + b_s^{(t)}), \\ Z_{(i,j)_k}^{(t)} &= v_i^{(t)} \oplus v_j^{(t)} \oplus u_{(i,j)_k} \end{aligned} \tag{6}$$

The terms in the sum operator represent the 2-body correlation of an atom with its neighboring atoms.

$Z^{(t)}_{(i,j)k}$ is the concatenation of the node and edge vectors. $\odot$ represents a matrix element-wise multiplication while σ and g respectively represent a sigmoid function and a nonlinear activation function. W^t and b^t are the weight and bias matrices respectively for the *t*-th convolution step. CGCNN offers a highly flexible framework to express different crystal structures and exhibits excellent performances in predicting a variety of material properties. In

this work, the CGCNN is utilized to train the nonlinear relationship between crystal structures and the Gruneisen parameter.

5. Predicting gruneisen parameter via CGCNN

5.1. Dataset collection

The training dataset is collected from the pubic AFLOW database[11], which has electron distribution, crystal structure, energy calculation, and novel material automatic prediction. It can also realize high-throughput calculation by online integration of VASP and QUANTUM ESPRESSO software. Furthermore, these calculation results can be stored in the database automatically, which can continuously expand by high-throughput calculations. Currently, the database has 106 orders of magnitude of different materials. In this work, we collected all binary compounds in the AFLOW as the training dataset, and inorganic binary and ternary compounds from the Materials Project as the testing dataset. However, the Gruneisen parameter of each material in the Materials Project is lacking and the calculation of it is prohibitive. Therefore, inspired by the rapid development of materials informatics, we train the CGCNN model to dig out the nonlinear mapping relationship between crystal structures and Gruneisen parameters from the available dataset. Thus one can quickly predict the Gruneisen parameter of multiple materials and avoid time-consuming computation. The dataset is obtained through the application programming interface (API) and the open-source Python Materials Genomics (pymatgen) materials analysis package for the AFLOW and the Materials Project. API provides permission based on Representative State Transfer (REST) principles to access material item data, such as density, volume, and crystal structures. In a RESTful system, information is organized into resources that can be uniquely identified by a Uniform Resource Identifier (URI). The use of identifiers allows the information corresponding to a certain material in the database to be extracted directly for subsequent use and processing, which provides the possibility of large-scale data access. We write a Python code to batch download the compound-10 related data and crystal structure files from the Materials Project database. In this way, we collected crystal structures of all needed compounds and their corresponding parameters from the AFLOW database and then used them as training data.

5.2. Hyperparameter setting

In this work, we tune hyperparameters by grid search during model training to achieve the best performance on our dataset. They are as follows: number of convolutional layers, length of atom feature vectors, length of hidden layer vectors, batchsize, learning rate, type of optimizer, the length of the layer, and regularization term. For training the larger theoretical dataset, cross-validation is done by randomly selecting 10% of the data as the validation set. For the small experimental dataset, a 5-fold cross-validation is used. In order to account for the random effect in training neural networks, each parameter is repeated 10 times during the training setting process. We use a deterministic grid search to optimize these hyperparameters and the optimal hyperparameters used in this work are listed in the following Table. SI.

TABLE. SI. The optimal hyperparameters used to train our crystal graph convolutional neural networks.

Type of neural network	Configurations and network parameters
Input layer	Crystal structure (.cif)
Number of convolutional layers	3
Length of atom feature vectors	64
Length of hidden layer vectors	128
Output layer	Gruneisen parameter
Loss function	MSELoss + regularization terms
Activation	ReLU for hidden layers, function linear for output layer
Regularization parameters	$\lambda = 0.1$
Maximum epochs	100
Batchsize	128
The ratio of training dataset	0.8
The ratio of validation dataset	0.1
The ratio of testing dataset	0.1

5.3. Model evaluation

After the model training process, we evaluate the performance of the model on the testing dataset. We take two standard evaluation metrics: R^2 and MAE (Mean Absolute Error) as our regression task, which is designed as follows. Assuming a set of samples $y = \{y_1, y_2, ..., y_n\}$ and the predicted dataset $y\hat{} = \{y_1\hat{}, y_2\hat{}, ..., y_n\hat{}\}$, where n is the number of sample dataset and wi represents the weight of each sample.

$$\mathrm{MAE} = \frac{1}{n}\sum_{i=1}^{n}\omega_i\left|y_i\hat{}-\bar{y}_i\right| \tag{7}$$

$$\mathrm{R}-Square = \frac{\sum_{\mathrm{i}=1}^{\mathrm{n}}\omega_i(y_i\hat{}-\bar{y}_i)^2}{\sum_{\mathrm{i}=1}^{\mathrm{n}}\omega_i(y_i-\bar{y}_i)^2} \tag{8}$$

The smaller the MAE value and the larger the R^2 value, the better the predictive performance of the model. The MAE denotes the average error between the model prediction and the true value. the smaller the MAE error, the better the model prediction performance. R^2 denotes the degree of fitting between the model prediction and the true value. the larger the value R^2, the better the model prediction fits the true value and the stronger the model generalization ability.

6.Predicting results of lattice thermal conductivity compared with experimental and AFLOW database

materials	ID-number	ρ	V	G	B	N	γ_{exp}	κ_{exp}	κ_{model}
AgCl [12]	mp-22922	5.36	44.43	7	43	2	1.9	1	0.80
Al_2O_3 [13]	mp-1143	3.87	87.42	147	232	10	1.34	30	38.45
AlAs [14]	mp-2172	3.59	47.13	39	70	2	0.66	98	44.05
AlN [14]	mp-661	3.2	42.53	122	194	4	0.7	350	119.24
AlP [14]	mp-1550	2.3	41.76	47	85	2	0.75	90	63.92
AlSb [14]	mp-2624	4.08	60.56	30	49	2	0.6	56	32.06
BaO [15]	mp-1342	5.75	44.26	38	68	2	1.5	2.3	14.15
BeO [14]	mp-2542	2.97	27.99	156	208	4	0.75	370	146.95
Bi_2Te_3 [16]	mp-34202	7.47	178.03	11	15	5	1.49	1.6	1.23
BN [14]	mp-1639	3.46	11.92	374	408	2	0.7	760	791.84
BP [14]	mp-1479	2.95	23.50	162	161	2	0.75	350	290.24
CaO [14]	mp-2605	3.29	28.33	74	105	2	1.57	30	40.46
CdS [14]	mp-672	4.58	104.86	18	53	4	0.75	16	7.41
CdSe [16]	mp-2691	5.3	59.95	15	45	2	0.6	4.4	10.11
CdTe [14]	mp-406	5.47	72.83	14	35	2	0.52	7.5	10.32
GaAs [14]	mp-2534	5.05	47.53	41	61	2	0.75	45	36.41
GaN [14]	mp-804	5.92	46.94	105	172	4	0.7	220	72.43
GaP [14]	mp-2490	4.01	41.74	52	76	2	0.75	100	55.84
GaSb [14]	mp-1156	5.29	60.13	30	45	2	0.75	40	24.09
Ge [14]	mp-32	5.04	47.85	45	59	2	1.06	65	30.63
InAs [14]	mp-20305	5.34	59.05	25	49	2	0.57	30	21.94
InP [14]	mp-20351	4.58	52.84	31	59	2	0.6	93	30.55
InSb [14]	mp-20012	5.38	72.96	19	35	2	0.56	20	15.66
KBr [14]	mp-23251	2.62	75.29	7	22	2	1.45	3.4	2.12
KCl [14]	mp-23193	1.9	65.03	9	16	2	1.45	7.1	3.39
KI [14]	mp-22898	2.97	92.74	6	10	2	1.45	2.6	1.66
LiF [14]	mp-1138	2.53	17.02	51	70	2	1.5	17.6	23.85
LiH [14]	mp-23703	0.82	16.00	43	37	2	1.28	15	38.69
NaBr [14]	mp-22916	3.12	54.75	12	27	2	1.5	2.8	3.69
NaCl [14]	mp-22862	2.11	46.10	14	23	2	1.56	7.1	4.97
NaF [14]	mp-682	2.69	25.89	30	48	2	1.5	18.4	12.08
NaI [14]	mp-23268	3.57	69.68	8	16	2	1.56	1.8	1.91
PbS [14]	mp-21276	7.33	54.17	29	52	2	2	2.9	5.42
PbSe [14]	mp-2201	7.89	60.25	27	47	2	2	2	4.86
RbBr [14]	mp-22867	3.16	86.78	6	14	2	1.45	3.8	1.59
RbCl [14]	mp-23295	2.67	75.19	8	15	2	1.45	2.8	2.52
RbI [14]	mp-22903	3.36	104.96	5	10	2	1.41	2.3	1.29
ZnO [14]	mp-2133	5.44	49.72	41	130	4	0.75	60	18.27
ZnS [14]	mp-10695	4	40.48	33	68	2	0.75	27	28.36
ZnSb [17]	mp-753	6.14	404.68	28	48	16	0.76	3.5	4.74

ZnSe [14]	mp-1190	5.06	47.34	28	58	2	0.75	19	20.77
ZnTe [14]	mp-2176	5.42	59.15	22	46	2	0.97	18	12.08

TABLE. SII. The comparison of the experimental thermal conductivity κ_L and predicted κ_L from our proposed model, all the unit of κ_L are W m^{-1} K^{-1}. More crystal structure information and properties can be found in the Materials Project database.

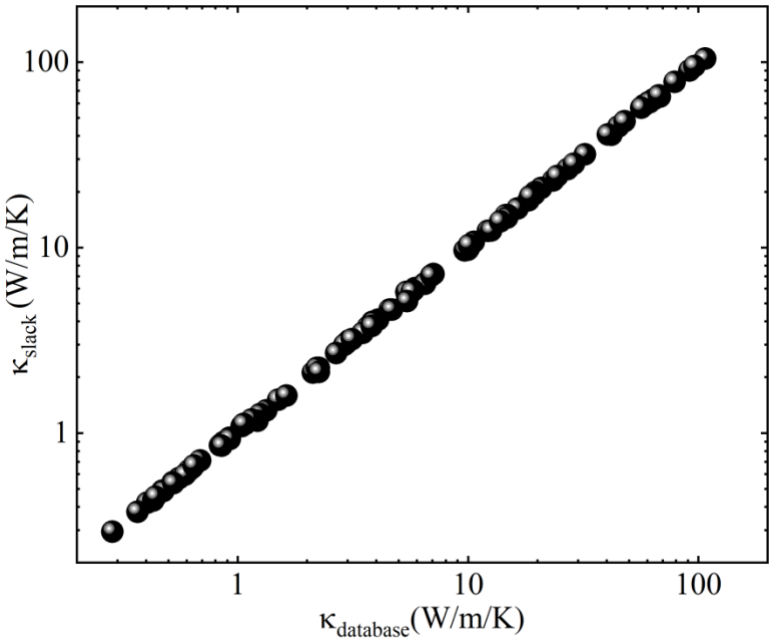

FIG. S2. Comparison between $\kappa_{database}$ from AFLOW database and κ_{slack} from Slack formula.

We randomly selected 100 data from AFLOW database and substituted corresponding parameters into Slack formula to get the thermal conductivity. The results are depicted in FIG. S2. In accordance with FIG. S2, there is no significant difference between AFLOW database and Slack's formula in terms of accuracy.

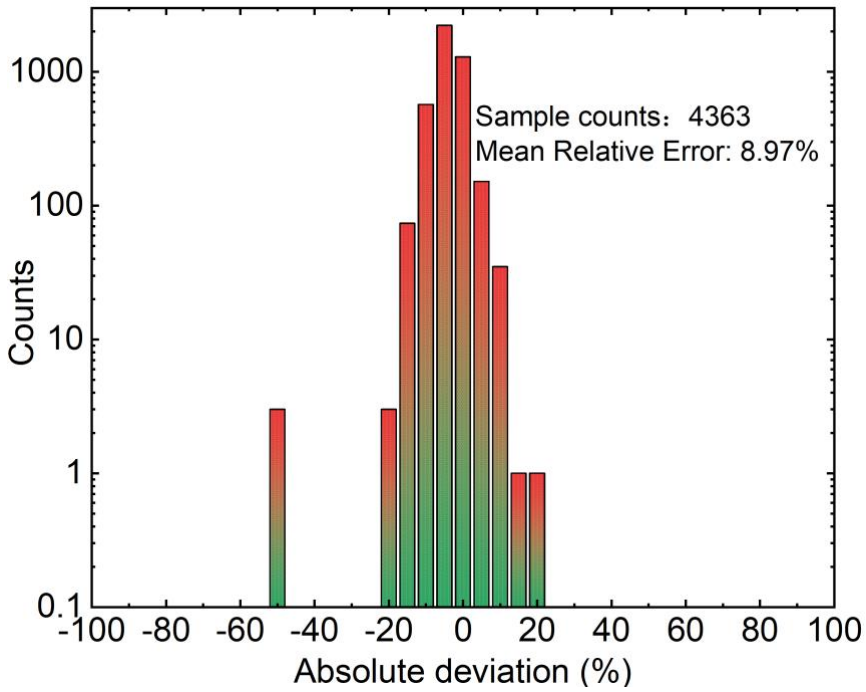

FIG. S3. Error analysis diagram for the predicted value of FIG.2 in manuscript of the thermal conductivity for AFLOW database. The horizontal coordinate represents the absolute deviation, and the vertical coordinate makes quantitative statistics in different error ranges. We use the mean relative error (MRE) to measure the gap between all the predicted values and the database values, the value is 8.97%. The formula to calculate MRE is: MRE= $\sum(|(x_{model} - y_{database}) / y_{database}|) / n \times 100\%$.

7. Application of our model

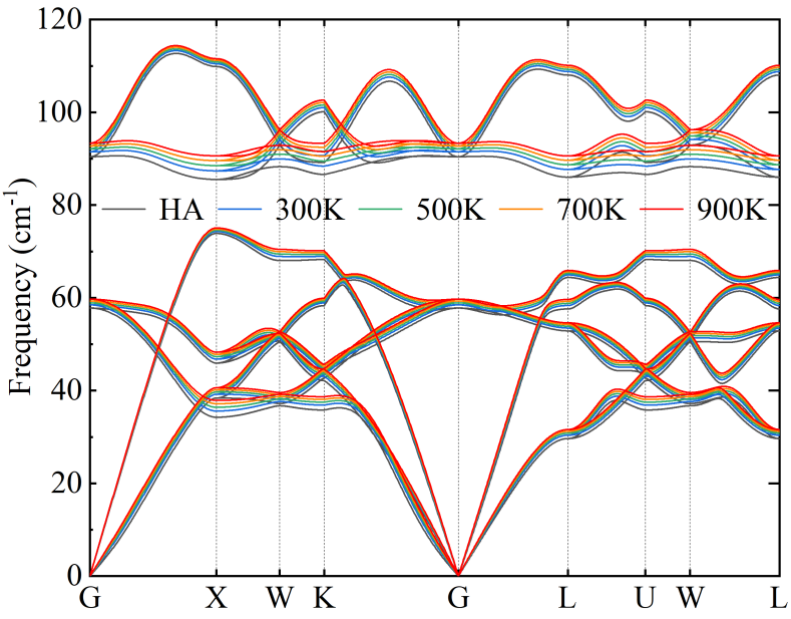

FIG. S4. The temperature-dependent colourful phonon spectrum for Cs_2Se from T = 300 K to 900 K using SCPH. The black line at T = 0 K denotes the harmonic approximation (HA).

According to the phonon dispersion at various temperatures. The temperature dependent phonon dispersion unquestionably reveals the stiffening of both acoustic and optical branches with increasing temperature.

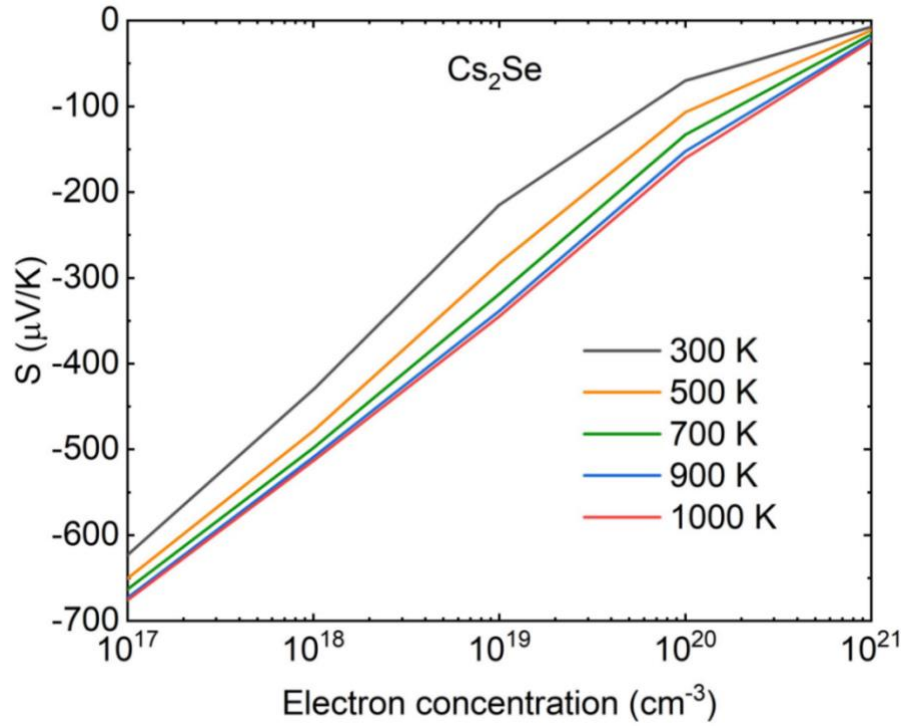

FIG. S5. The transport performance of the Seebeck coefficient for n-type Cs_2Se at 300 K, 500 K, 700 K, 900 K, and 1000 K, respectively.

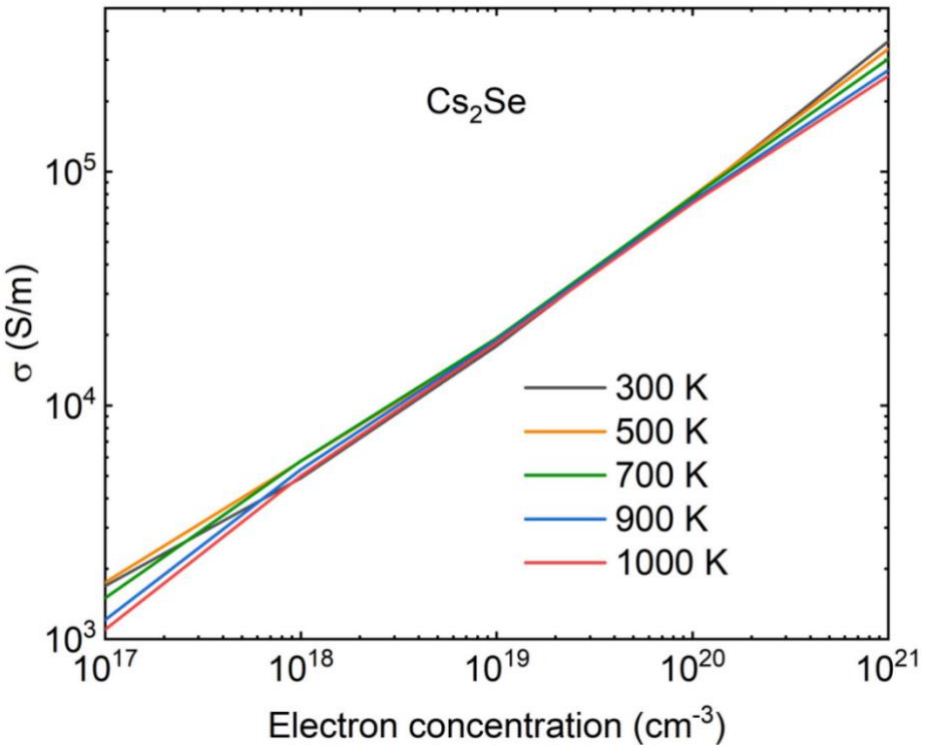

FIG. S6. The transport performance of electronic conductivity for n-type Cs_2Se at 300 K, 500 K, 700 K, 900 K, and 1000 K, respectively.

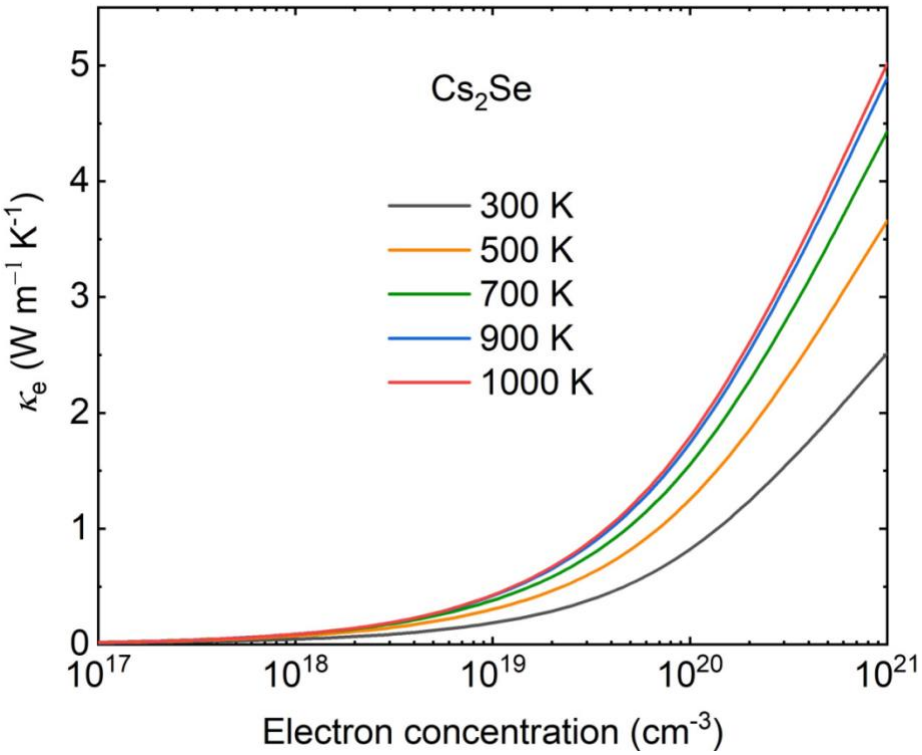

FIG. S7. The transport performance of electronic thermal conductivity for n-type Cs_2Se at 300 K, 500 K, 700 K, 900 K, and 1000 K, respectively.

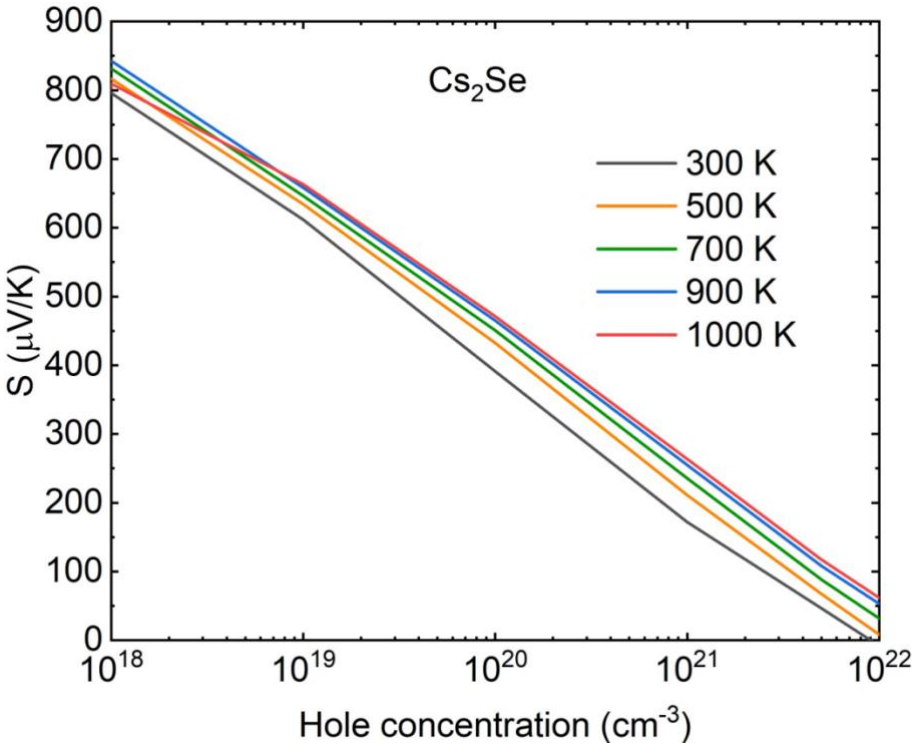

FIG. S8. The transport performance of the Seebeck coefficient for p-type Cs_2Se at 300 K, 500 K, 700 K, 900 K, and 1000 K, respectively.

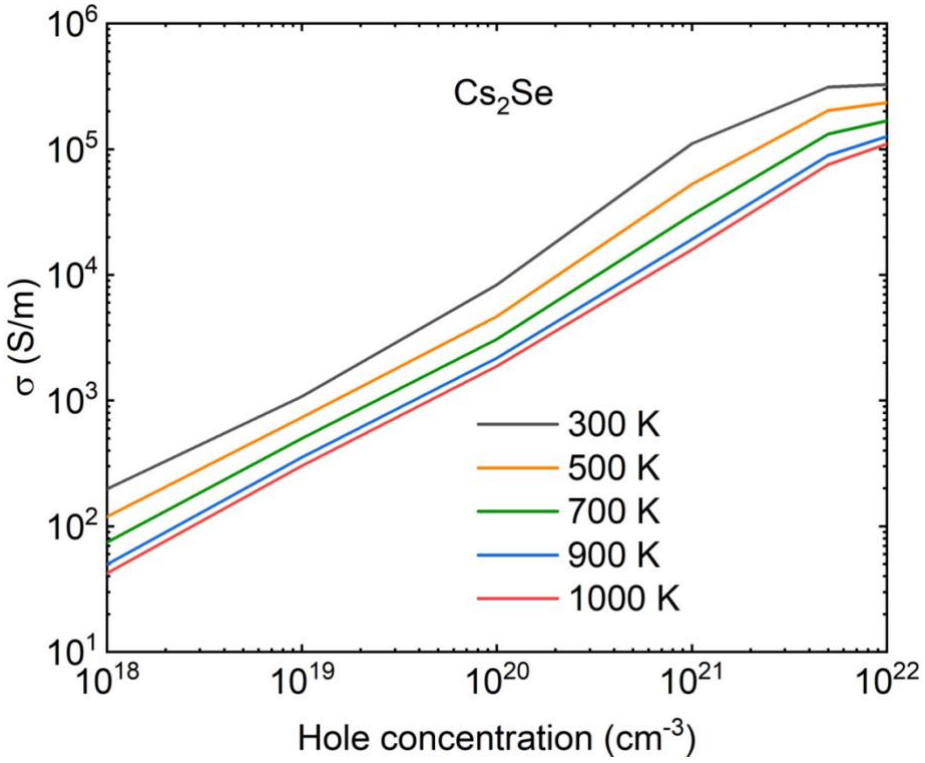

FIG. S9. The transport performance of electronic conductivity for p-type Cs_2Se at 300 K, 500 K, 700 K, 900 K, and 1000 K, respectively.

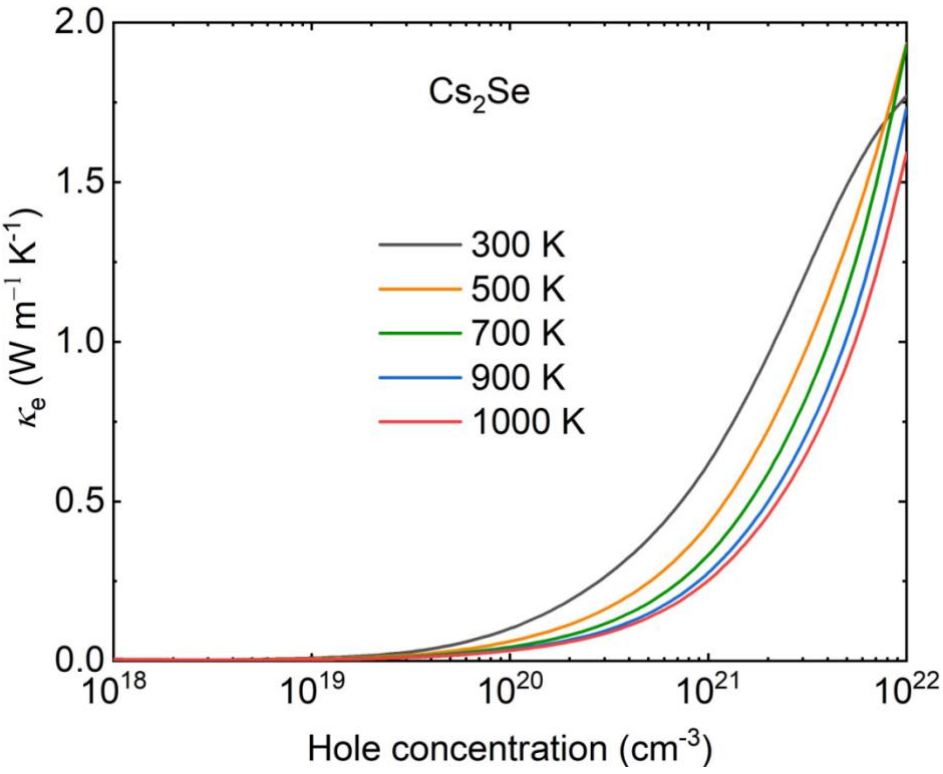

FIG. S10. The transport performance of electronic thermal conductivity for p-type Cs_2Se at 300 K, 500 K, 700 K, 900 K, and 1000 K, respectively.

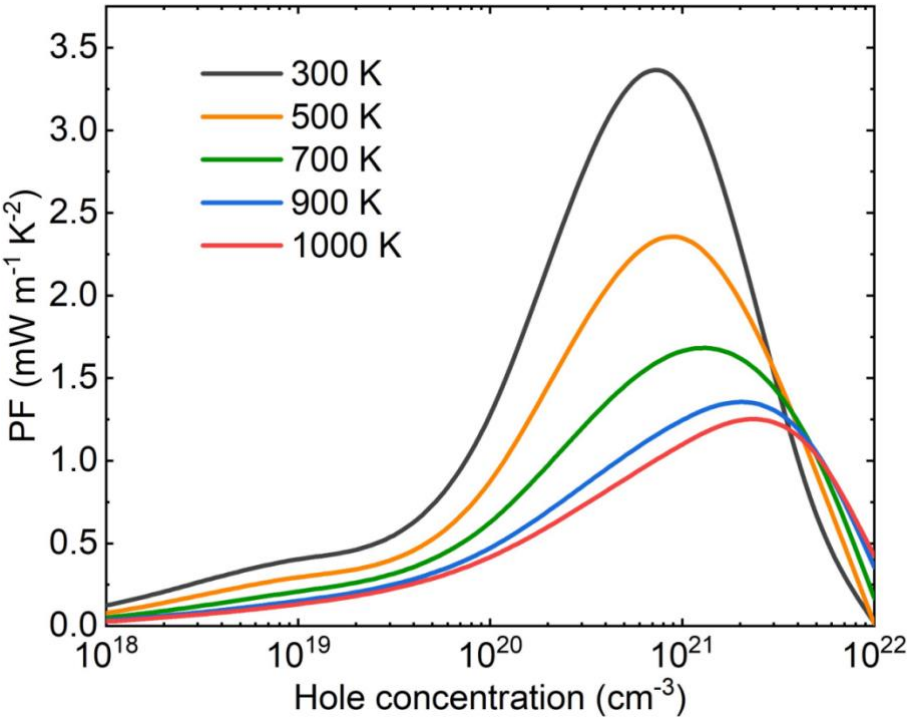

FIG. S11. The transport performance of power factor (*PF*) for p-type Cs_2Se at 300 K, 500 K, 700 K, 900 K, and 1000 K, respectively.

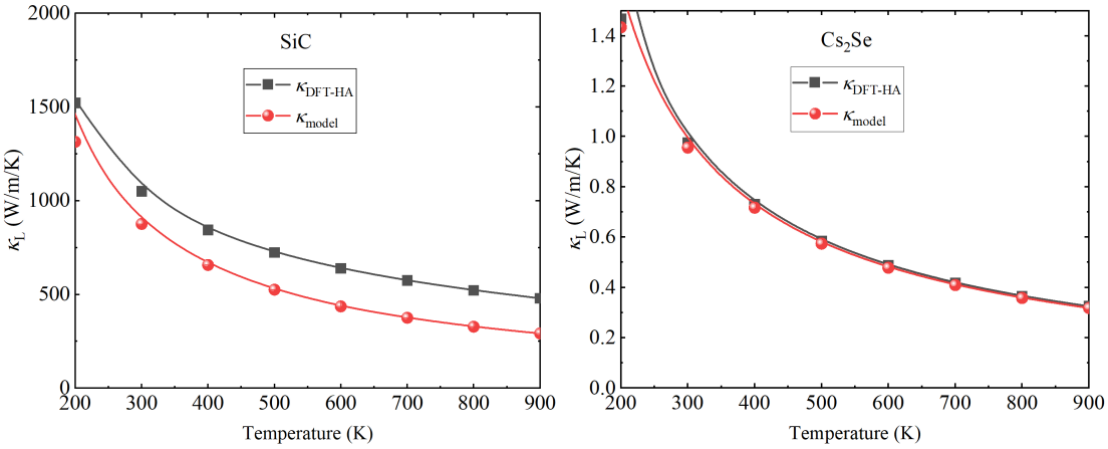

FIG. S12. Comparison between $k_{DFT\text{-}HA}$ by harmonic approximation using VASP calculation and k_{model} from our formula applying over a large temperature range.

In order to verify the universality at different temperatures. We plug the formula into a wider range of temperatures from 200 K to 900 K. We apply our formula into a kind of high thermal conductivity material SiC and a kind of low thermal conductivity material Cs_2Se with various temperatures as FIG. S12. According to these two materials, it seems that our formula can be applied to Cs_2Se better. Because the Gruneisen constant is a temperature-dependent parameter, the gruneisen parameter of SiC at 200 K is 0.51, however, it increases to 0.80 at 800 K. For Cs_2Se, the gruneisen parameter is 1.36 at 200 K, even at 800 K, the gruneisen parameter is 1.28. Therefore, due to the temperature

dependence of γ, our formula is applicable to a large temperature range for materials with little change in Grineisen parameter with temperature, while for materials with large change in Grineisen parameter with temperature, the prediction results are for reference only. We may conduct research on this formula in a large temperature range in the future.

References:

[1] Werthamer, N. R. Self-consistent phonon formulation of anharmonic lattice dynamics, *Phys. Rev. B*, **1**, 572 (1970).

[2] Tadano, T., & Tsuneyuki, S. Self-consistent phonon calculations of lattice dynamical properties in cubic $SrTiO_3$ with first-principles anharmonic force constants. *Phys. Rev. B*, **92**, 054301 (2015).

[3] Xia, Y., Hegde, V. I., Pal, K., Hua, X., Gaines, D., Patel, S., ... & Wolverton, C. High-throughput study of lattice thermal conductivity in binary rocksalt and zinc blende compounds including higher-order anharmonicity. *Phys. Rev. X*, **10**, 041029 (2020).

[4] Wang, X., Gao, Z., Zhu, G., Ren, J., Hu, L., Sun, J., ... & Li, B. Role of high-order anharmonicity and off-diagonal terms in thermal conductivity: A case study of multiphase $CsPbBr_3$. *Phys. Rev. B*, **107**, 214308 (2023).

[5] Kresse, G., & Furthmü ller, J. Efficient iterative schemes for ab initio total-energy calculations using a plane-wave basis set. *Phys. Rev. B*, **54**, 11169 (1996).

[6] Perdew, J. P., Burke, K., & Ernzerhof, M. Generalized gradient approximation made simple. *Phys. Rev. Lett*. , **77**, 3865 (1996).

[7] Togo, A., & Tanaka, I. First principles phonon calculations in materials science. *Scripta Materialia*, **108**, 1-5 (2015).

[8] Zhou, F., Nielson, W., Xia, Y., & Ozoliņš, V. Lattice anharmonicity and thermal conductivity from compressive sensing of first-principles calculations. *Phys. Rev. Lett.* , **113**, 185501 (2014).

[9] Han, Z., Yang, X., Li, W., Feng, T., & Ruan, X. FourPhonon: An extension module to ShengBTE for computing four-phonon scattering rates and thermal conductivity. Comput. Phys. Commun., **270**, 108179 (2022).

[10] Xie, T., & Grossman, J. C. Crystal graph convolutional neural networks for an accurate and interpretable prediction of material properties. *Phys. Rev. Lett*., **120**, 145301 (2018).

[11] Curtarolo, S., Setyawan, W., Hart, G. L., Jahnatek, M., Chepulskii, R. V., Taylor, R. H., ... & Morgan, D. AFLOW: An automatic framework for high-throughput materials discovery. *Com. Mat. Science* **58**,218-226 (2012).

[12] Beasley, J. D. Thermal conductivities of some novel nonlinear optical materials. *Appl. Opt*. **33,** 1000 (1994).

[13] Slack, G. A. Thermal conductivity of MgO, Al_2O_3, $MgAl_2O_4$, and Fe_3O_4 crystals from 3° to 300° K. *Phys. Rev.* **126,** 427 (1962).

[14] D. T. Morelli and G. A. Slack, High lattice thermal conductivity solids, in High Thermal Conductivity Materials, edited by S. L. Shindé and J. S. Goela (*Springer, New York*, 2006), pp. 37-68.

[15] Surplice, N. A., & Jones, R. P. The thermal conductivity of alkaline earth oxides. British.

J. Appl. Phys., **14**, 720 (1963).
[16] Toberer, E. S., Zevalkink, A., & Snyder, G. J. Phonon engineering through crystal chemistry. *J. Mater. Chem.*, **21**, 15843-15852 (2011).
[17] Bjerg, L., Iversen, B. B., & Madsen, G. K. Modeling the thermal conductivities of the zinc antimonides ZnSb and Zn_4 Sb_3. *Phys. Rev. B*, **89**, 024304 (2014).